CHEMISTRY OF MATERIALS

pubs.acs.org/cm

Article

Mechanochemical Synthesis and Thin-Film Deposition of Zero-Dimensional Cesium Lead Mixed-Halide Perovskites for Wide-Range Color-Tunable Emission

Hyungbin Lim,[▽] Kyeong-Yoon Baek,[▽] Jae Il Kim, Jonghoon Lee, Jaeyoung Kim, Heebeom Ahn, Hyeonmin Choi, Seung-Je Woo, Sung Keun Lee, Tae-Woo Lee, Jeongjae Lee,* Keehoon Kang,* and Takhee Lee*

Cite This: https://doi.org/10.1021/acs.chemmater.3c00833

Read Online

ACCESS | Metrics & More | Article Recommendations | Supporting Information

ABSTRACT: Metal-halide perovskites possess synthetic tunability in terms of their compositions and structures, which results in a facile control of the properties crucial for optoelectronic device applications. For instance, the optical band gap of perovskites can be adjusted by means of halide compositions, which can generate a wide range of perovskite phases emitting visible light from purple to red. Furthermore, embedding the emissive perovskites within inorganic structural matrices provides further opportunities to tune their functionalities. In this study, we demonstrate that mechanochemical synthesis (MCS) can be successfully employed to prepare a full range of mixed-halide zero-dimensional (0D) perovskites ($Cs_4PbCl_mBr_{6-m}$ and $Cs_4PbBr_{6-m}I_m$, where m is an integer from 0 to 6). The synthesized mixed-halide 0D perovskite powder samples exhibited photoluminescence emissions spanning the entire visible spectrum (410−690 nm), which likely originates from the inclusion of three-dimensional perovskites. Furthermore, we demonstrate that our 0D perovskite powder samples can be readily used as the source for fabricating thin films via fast single-source vacuum deposition while preserving the optical properties of the source powder samples. Overall, our study reveals the versatility of MCS as a useful toolkit for preparing a family of 0D perovskites with a full range of halide compositions with potential for light-emitting applications.

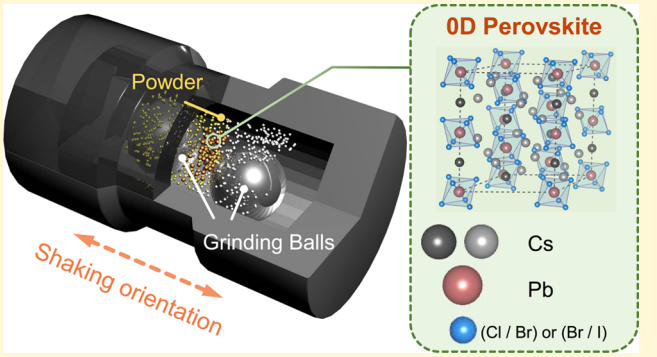

1. INTRODUCTION

Lead halide perovskites have emerged as promising classes of materials for various optoelectronic devices, such as light-emitting diodes,[1−4] solar cells,[5−8] and photodetectors[9] due to their high photoluminescence (PL) quantum efficiency (QE), narrow full width at half-maximum (FWHM), and tunable band gap.[10−13] A range of perovskite structures can be formed by means of varying the interconnections of the basic building blocks of these perovskites, the octahedron $[PbX_6]^{4-}$, where X stands for halide anions (i.e., Cl^-, Br^-, or I^-). Moreover, the electronic structures of these perovskites can be further tuned by changing the halide compositions.[14] Conventionally, three-dimensional (3D) perovskites, which are composed of extended network of corner-sharing octahedra, have been widely studied owing to their attractive optical properties emerging from the direct band gap, high absorption coefficient, and the potential to cover the entire visible light spectrum by mixing the halide species.[10−12] However, 3D perovskites typically suffer from ion migration, surface degradation, and low photostability under an ambient environment. Hence, it is often necessary to encapsulate 3D perovskite nanocrystals with host matrices, such as organic ligands,[15] metal−organic frameworks,[16] or low-dimensional perovskites,[17,18] which can protect the 3D emitters and preserve their emission properties.

In particular, the discovery of serendipitous inclusion of 3D perovskite nanocrystals within zero-dimensional (0D) perovskites, which are composed of completely isolated octahedra, has drawn attention to possibilities for such encapsulation using inorganic hosts. Cs_4PbBr_6, a type of 0D perovskite, emits not only the intrinsic ultraviolet (UV) light corresponding to its band gap (~3.9 eV) but also stable green light (~513 nm) with narrow FWHM (~19 nm) and high PLQE (~90%) favorable for optoelectronic applications; a series of experimental studies suggests that 3D perovskite ($CsPbBr_3$) nanoparticles embedded in a 0D perovskite (Cs_4PbBr_6) matrix are the source of this green

Received: April 9, 2023
Revised: July 1, 2023

light with long-term stability.[19−22] Similarly, other 0D perovskites, Cs_4PbCl_6 and Cs_4PbI_6, have also been reported to emit purple and red light originating from the 3D perovskite nanocrystals, $CsPbCl_3$ and $CsPbI_3$, embedded in a 0D perovskite, respectively.[23,24] Since the light emission of 0D perovskites likely originates from the 3D perovskite crystals which are embedded by virtue of lattice matching in the host matrix, the emission wavelength was tuned by simultaneously controlling the halide ratio of the 3D perovskite in the 0D matrix by controlling the halide ratio of the host 0D perovskite (see Section 1.1 in the Supporting Information).

However, structural information that determines the emission properties of the mixed-halide 0D perovskites has been limited in many aspects: namely, (1) the discrepancy between nominal and actual macroscopic halide compositions, (2) the exact local halide distribution (i.e., Pb−X local bonding environment), and (3) the extent of 3D crystal inclusion within the 0D matrix (i.e., the origin of the visible light emission). Ideally, to achieve narrow emission in mixed halides, the individual halide ions must be uniformly distributed within the halide sublattice without any halide segregation or clustering which gives rise to broad emission peaks composed of multiple wavelengths. However, perovskite samples produced through solvent synthesis typically show such halide segregation due to the "freezing" tendency of halide ions in their solvation environment in precursor solutions upon crystal growth.[25,26] Moreover, optimal synthesis protocols to produce Cl/Br[27] or Br/I[28] often differ from each other, whereas it would be desirable to develop a single method for large-scale production of perovskite samples across multiple wavelengths. Therefore, a unified synthetic method for both Cl/Br and Br/I perovskite systems is highly sought after, which would allow fine tuning of halide ratios of the perovskite powder samples to achieve emissions spanning across the whole range of visible light.

In this study, we present mechanochemical synthesis (MCS), a solvent-free method to prepare solid-state powder samples,[29,30] as a means of preparing the full family of mixed-halide Cs_4PbX_6 perovskites along the entire halide composition range ($Cs_4PbCl_mBr_{6-m}$ and $Cs_4PbBr_{6-m}I_m$, where m is an integer from 0 to 6). Unlike solvent-based synthesis, MCS can continuously apply a physical force to the powder samples during the entire synthetic process, resulting in better homogenization of the different halide atoms in the halide sublattice and more uniform halide distribution. Our synthesized 0D perovskite powder samples exhibit the full range of visible light from purple to red (410−690 nm) with narrow FWHMs (17−60 nm) depending on the halide ratios, which likely arises from the potential inclusion of the 3D perovskite nanocrystals in the 0D perovskite matrices over the full range of halide compositions from Cl to Br to I. Finally, we demonstrate that these powder samples can be deposited into thin films by employing the single-source vacuum deposition method accompanied with a postannealing process, which provides a straightforward powder synthesis and film deposition protocol for fabricating emissive mixed-halide 3D@0D perovskite films with their emission across the entire visible spectral region.

2. EXPERIMENTAL SECTION

2.1. Sample Preparation. Cesium chloride (CsCl, 98%), cesium bromide (CsBr, 99.9%), cesium iodide (CsI, 99.9%), lead chloride ($PbCl_2$, 98%), lead bromide ($PbBr_2$, 98%), and lead iodide (PbI_2, 99%) salts were purchased from Sigma-Aldrich. All chemicals were used as received without further purification. The molar fraction of the precursors was modulated in respect to the desired halide stoichiometric ratio of the mixed-halide 0D perovskites with a fixed total mass of 2.278 g. Then, the precursor salts were put in a stainless-steel jar with two stainless-steel grinding balls (28.65 g and 1.9 cm in diameter). The jar was vigorously shaken with a shaker-type ball mill (Mixer Mill MM-400, Retsch) at 17 Hz for 3 h. The synthesized perovskite powder samples were stored in a nitrogen-filled glovebox.

The synthesized perovskite powder samples were used to form perovskite films. The perovskite film deposition was performed on three types of substrates (270 nm SiO_2 on silicon, silicon, and glass). The substrates were sequentially cleaned with acetone, isopropyl alcohol, and deionized water in a sonicator for 10 min each. Then, the substrates were exposed to O_2 plasma using the reactive-ion etching technique (power of 50 W, flow of 30 cm^3/min, and duration of 120 s) to generate hydrophilic surfaces. As for single-source vacuum deposition, the synthesized perovskite powder samples were loaded in a tungsten boat. The cleaned substrates were placed in a vacuum chamber at a height of 30 cm from the boat. The chamber was evacuated to 5×10^{-6} Torr, and the tungsten boat was rapidly heated by applying a current of 140 A. The source samples were fully evaporated within 30 s. After the deposition, the perovskite films were thermally annealed at 150 °C in 1×10^{-4} Torr vacuum for 5 min.

2.2. Structural Characterization. High-resolution X-ray diffraction (XRD) measurements for perovskite films and powder XRD (PXRD) measurements for perovskite powder samples were performed with a Rigaku SmartLab diffractometer utilizing 9 kW and 3 kW X-ray generators, respectively. Rietveld refinement was performed using GSAS-II software.[31] ^{133}Cs solid-state nuclear magnetic resonance (ssNMR) spectra were obtained using 3.2 mm cross-polarization magic angle spinning (MAS) probes in a 600 MHz Bruker AVANCE III NMR spectrometer with a spinning speed of 22 kHz at 14.1 T. Rotor-synchronized Hahn echo sequence was used to minimize baseline distortion. Additional ^{133}Cs ssNMR spectra at a lower field were obtained using 4 mm cross-polarization MAS probes in a 500 MHz Bruker AVANCE III HD NMR spectrometer with a spinning speed of 10 kHz at 11.7 T. All ^{133}Cs spectra were referenced using a secondary reference of solid CsBr (260.3 ppm), which corresponds to the primary reference of aqueous CsCl (0 ppm). A simple pulse-acquire sequence was used with a flip angle of 20° with 52 kHz radiofrequency amplitude. Raman spectra of the mixed-halide 0D perovskite powder samples were measured through a confocal imaging system (DXR2xi, Thermo Scientific) using an incident laser beam with a wavelength of 785 nm. The field-emission scanning electron microscope (FE-SEM) images and energy-dispersive spectroscopy (EDS) mapping images of the samples were obtained using a JSM-7800F Prime (JEOL Ltd.) at acceleration voltages of 15 and 10 kV, respectively.

2.3. Optical Characterization. Steady-state PL emission spectra were measured using a spectrofluorometer (FP-8500, JASCO) with a Xenon arc lamp. PLQE was measured utilizing the same spectrofluorometer equipped with a 100 mm integrating sphere (ILF-835) coated with barium sulfate and the value was calculated using JASCO Spectra Manager II software. 10 mg of the synthesized powder samples was dispersed in 10 mL of toluene, or the powder samples were diluted in a UV-hardening resin for PLQE measurements. Power-dependent PL intensity plots were obtained through a Nanobase XperRam using the incident laser beams with a wavelength of 405 nm for the $Cs_4PbCl_mBr_{6-m}$ powder samples and a wavelength of 532 nm for the $Cs_4PbBr_{6-m}I_m$ powder samples. Absorption spectra were obtained by measuring the reflectance spectra of the samples using a UV−vis spectrophotometer (V-770, JASCO) equipped with a 150-mm integrating sphere (ILN-925) coated with barium sulfate. A 365 nm light-emitting diode (LED) (LZ4-V4UV0R-0000) and a 395 nm LED (SBM-120-UV-R34-L395−22) were used as backlights of color-conversion perovskite films. Emission spectra were measured by a charge-coupled device (CCD) spectrometer (Maya 2000, Ocean Optics).

https://doi.org/10.1021/acs.chemmater.3c00833
Chem. Mater. XXXX, XXX, XXX−XXX

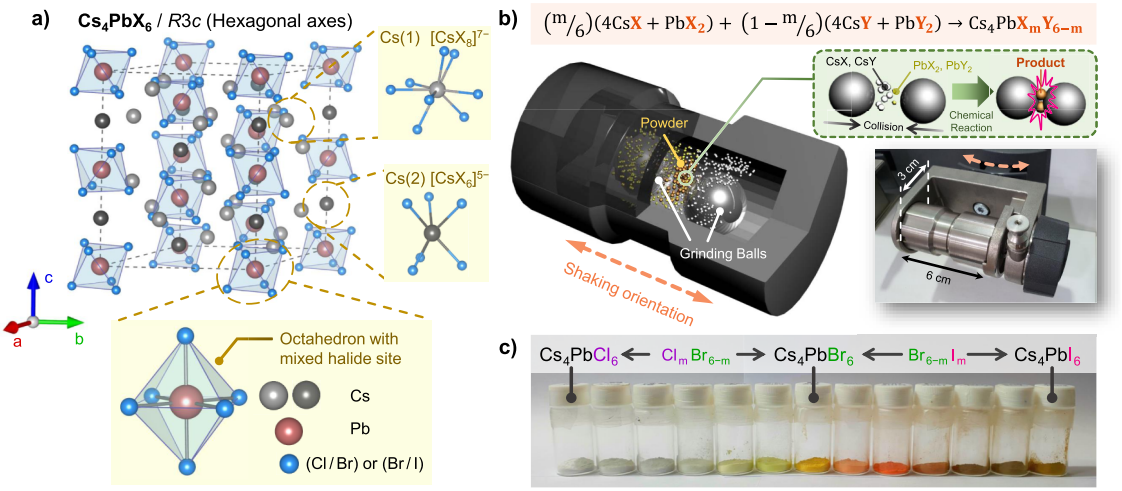

Figure 1. (a) Schematic illustration of the Cs_4PbX_6 crystal structure. The inset at the bottom is a schematic of the $[PbX_6]^{4-}$ octahedron, and the insets on the right show the $[CsX_8]^{7-}$ and $[CsX_6]^{5-}$ structures. (b) Schematic illustration of the shaker-type MCS procedure for producing mixed-halide 0D perovskite powder samples. The reaction formula shown in the orange-filled box and the schematic in the green-filled box illustrate the chemical reaction. The image at the bottom right shows a photograph of the MCS setup. (c) Photographs of the powder samples synthesized through the process portrayed in panel (b). Cs_4PbCl_6 to Cs_4PbI_6 are shown from left to right with a successive change in the halide coordinate, integer m.

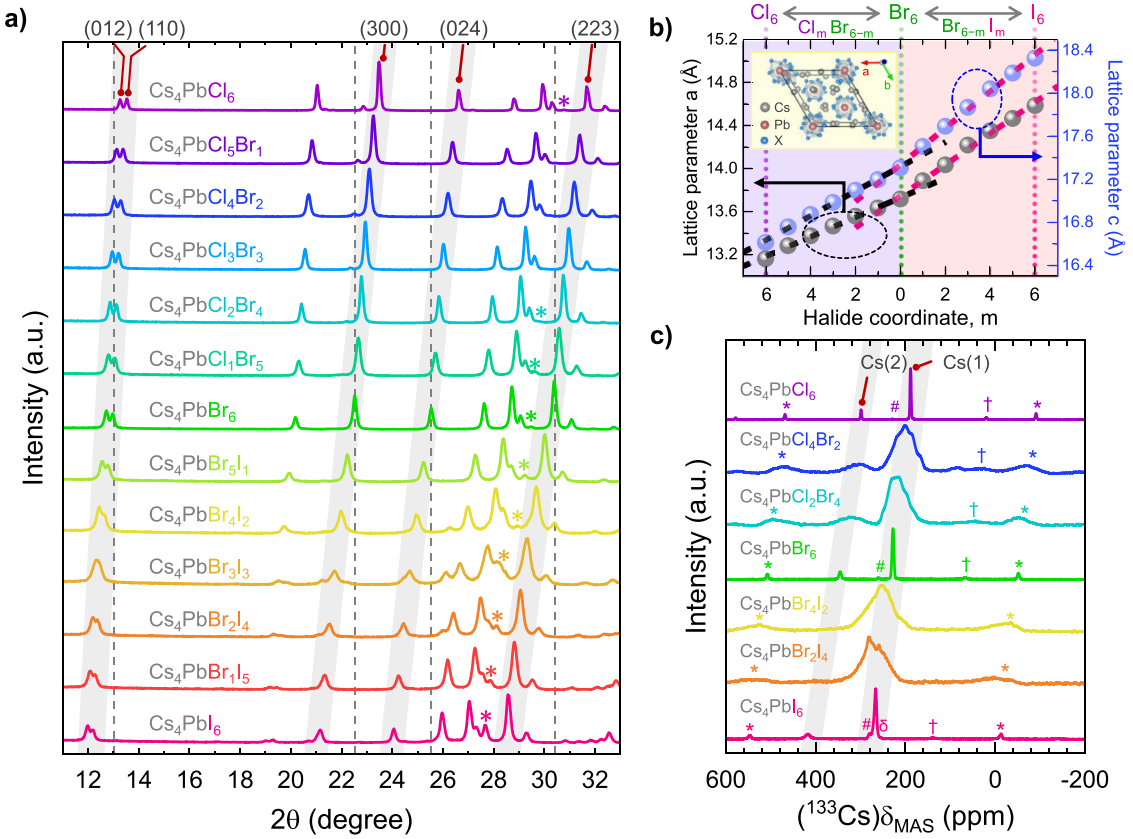

Figure 2. (a) PXRD patterns of the mixed-halide 0D perovskite powder samples. The representative lattice planes are marked as semitransparent gray stripes, and the asterisks (*) indicate CsX impurities (X is a halide element). The dashed gray lines are (012), (110), (300), (024), and (223) planes of Cs_4PbBr_6. (b) Lattice parameters of each sample calculated from the results of the PXRD patterns in panel (a). We adopted the same unit cell standard presented in Figure 1a which is on the basis of the hexagonal axes. The unit cell viewed from the c-axis of the hexagonal plane is portrayed in the yellow-filled box in the inset. (c) ^{133}Cs ssNMR spectra of each sample at 22 kHz MAS and 300 K. Two different Cs environments, namely, Cs(1) and Cs(2), are marked as semitransparent gray stripes. The hashtag (#), delta (δ), asterisk (*), and dagger (†) indicate CsX (X is a halide element), δ-$CsPbI_3$ (nonperovskite phase), spinning side bands of Cs(1) peak, and spinning side bands of Cs(2) peak, respectively.

https://doi.org/10.1021/acs.chemmater.3c00833
Chem. Mater. XXXX, XXX, XXX−XXX

3. RESULTS AND DISCUSSION

3.1. Synthesis and Characterization of Mixed-Halide 0D Perovskites through the MCS Method. Figure 1a shows the schematic illustration of the 0D perovskite crystal structure which is in the hexagonal space group $R\bar{3}c$ (space group number 167). Each $[PbX_6]^{4-}$ octahedron is not connected with one another, and Cs^+ atoms reside in the voids between the octahedra, balancing out the Coulombic force and maintaining the crystal structure.[32] The inset shown at the bottom of Figure 1a is a schematic of one of the $[PbX_6]^{4-}$ octahedra. The right insets of Figure 1a show the $[CsX_8]^{7-}$ structure with a light gray Cs atom and the $[CsX_6]^{5-}$ structure with a dark gray Cs atom, which represents the two different Cs environments (labeled as Cs(1) and Cs(2), respectively).[33] In this study where we focus on the 0D perovskite with mixed-halide sites, the halogen atoms in the vertex of each octahedron are composed of either Cl or Br, or either Br or I. Note that the mixing of Cl and I on the halide sublattice is not feasible due to the large difference in their ionic radii.[10,11]

Figure 1b portrays the shaker-type ball-milling method that we employed to produce the mixed-halide 0D perovskite powder samples. In this study, 13 powder samples of composition $Cs_4PbX_mY_{6-m}$ (X and Y are the halide elements among Cl, Br, and I and m is an integer from 0 to 6 which represents the halide coordinate) were prepared from precursor salts of CsX and PbX_2, and CsY and PbY_2 each with a stoichiometric ratio of 4 to 1 (see the orange-filled box of Figure 1b). A cylinder-shaped jar made of stainless steel, loaded with the precursor powder samples and two grinding balls, was mechanically vibrated at a frequency of 17 Hz for 3 h along the longitudinal direction. As shown in the green-filled box of Figure 1b, vigorously shaking the contents in the jar results in repeated collisions between the grinding balls and the jar wall, which provides enough mechanical energy for the precursors to initiate the solid-state chemical reaction. Along the composition line of Cs_4PbX_6 with the successive substitution of X = Cl to Br and Br to I, the 13 samples exhibit a gradual change in color from white to orange to dark brown under white light (Figure 1c), which indicates tuning of the underlying electronic structure (see below).

The formation of 0D perovskite powder samples with mixed-halide compositions through shaker-type MCS was confirmed with a series of analytical techniques: PXRD, FE-SEM, EDS, ssNMR, and Raman spectroscopy. PXRD measurements were performed on all 13 samples to ascertain the successful synthesis of 0D perovskite and the evolution of lattice parameters upon halide mixing. The resulting powder diffraction pattern for the monohalide end-member compositions Cs_4PbCl_6, Cs_4PbBr_6, and Cs_4PbI_6 shown in Figure 2a clearly demonstrates the formation of hexagonal 0D perovskite structures, as displayed in Figure 1a, where the lattice parameters match the reported values for each phase[23,34,35] (see the Supporting Information, Figure S1). Note that the small peaks marked with asterisks in Figure 2a indicate the presence of CsX. Regarding the mixed-halide intermediate-member compositions, a prominent trend of decreasing 2θ angles is made evident with the increase of Br/Cl ratio for the $Cs_4PbCl_mBr_{6-m}$ samples and I/Br ratio for the $Cs_4PbBr_{6-m}I_m$ samples. Although this progression is universal for all lattice plane reflections, it was particularly evident for the representative lattice planes (012), (110), (300), (024), and (223) of each sample (marked as semitransparent gray stripes). This expansion of lattice parameters, which originates from the gradual substitution of smaller halide atoms with bigger halide atoms (i.e., substitution of Cl with Br and substitution of Br with I), strongly suggests the formation of 0D perovskite phases with mixed-halide compositions and precludes the existence of a mixture of two single-halide end-member phases.[27,36] Values of the lattice parameters for all 13 samples determined from Rietveld refinements of the PXRD patterns are shown on Figure 2b. The observed linear evolution of the lattice parameters for the $Cs_4PbCl_mBr_{6-m}$ and $Cs_4PbBr_{6-m}I_m$ samples clearly indicates the presence of mixed-halide 0D perovskite with the intended halide ratios. The slope difference between the dashed black line and the dashed red line is attributed to the difference between the ionic radii of Cl^- (1.81 Å) and Br^- (1.96 Å) and those of Br^- and I^- (2.20 Å), respectively.[37] FE-SEM and EDS elemental mapping images shown in Figure S2 also exhibit a uniform spatial distribution of multiple halide elements, thereby supporting the formation of mixed-halide 0D perovskites.

In order to confirm the halide mixing on an atomistic scale and to probe the possible presence of other (amorphous) products, ^{133}Cs MAS ssNMR measurements were performed on the representative mixed-halide samples $Cs_4PbCl_4Br_2$, $Cs_4PbCl_2Br_4$, $Cs_4PbBr_4I_2$, and $Cs_4PbBr_2I_4$, as well as the monohalide perovskites Cs_4PbCl_6, Cs_4PbBr_6, and Cs_4PbI_6 for references (Figure 2c). For the three monohalide composition perovskites, presence of two distinct Cs environments in the 0D perovskites, as shown in the PXRD structures (Figure 1a),[33] is evident on the NMR spectra as two sharp isotropic resonances, highlighted with semitransparent gray stripes in Figure 2c. The ^{133}Cs chemical shifts (δ_{iso}) of the two cesium sites Cs(1) and Cs(2) in all of these compounds exhibit monotonic increases to higher chemical shifts as the halide atomic number increases (from Cl to I). This trend, which is consistent with the trend observed in crystalline halides CsX (X = Cl, Br, I),[38] may be rationalized by correlating the decreasing band gap in the cesium halides to the Ramsey theory of chemical shifts.[39] In addition, the narrow peak widths in these series of spectra allow high-resolution identification of the trace-level Cs environments present in these samples: all three spectra exhibit peaks arising from CsX precursors (marked with hashtags). A peak at 253 ppm is also seen on the spectrum of the Cs_4PbI_6 sample, and it is attributed to the nonperovskite δ-$CsPbI_3$ phase (marked with a delta). Controlling the inclusion proportion of this undesired δ-phase nonperovskite will be discussed later in the discussion of the deposition of perovskite films. Note that no traces of peaks corresponding to emissive 3D perovskite $CsPbX_3$ are observed for all three spectra, indicating that their concentrations were below the detection limit of NMR (and PXRD) but enough to give PL emission.[22]

On the other hand, the ^{133}Cs spectra of mixed-halide systems are markedly different from the above discussed monohalide cases. The Cs peaks are significantly broadened to the extent that only the Cs(1) and Cs(2) sites in the 0D perovskite (the majority phase), highlighted in semitransparent gray stripes, are reliably resolved; all other potential Cs peaks are now buried below the broad humps. These characteristic broad Cs(1) and Cs(2) peaks are readily interpreted in terms of local halide site disorder in mixed-halide systems, which is indicated by $[CsX_xY_{8-x}]^{7-}$ for Cs(1) and $[CsX_xY_{6-x}]^{5-}$ for Cs(2). The observed broadening must be ascribed to different chemical environments originating from the distinct local halide coordination, where the probabilities of finding individual Cs species should follow a binomial distribution depending on the bulk halide composition.[25,26,40] Such random distribution must

https://doi.org/10.1021/acs.chemmater.3c00833
Chem. Mater. XXXX, XXX, XXX−XXX

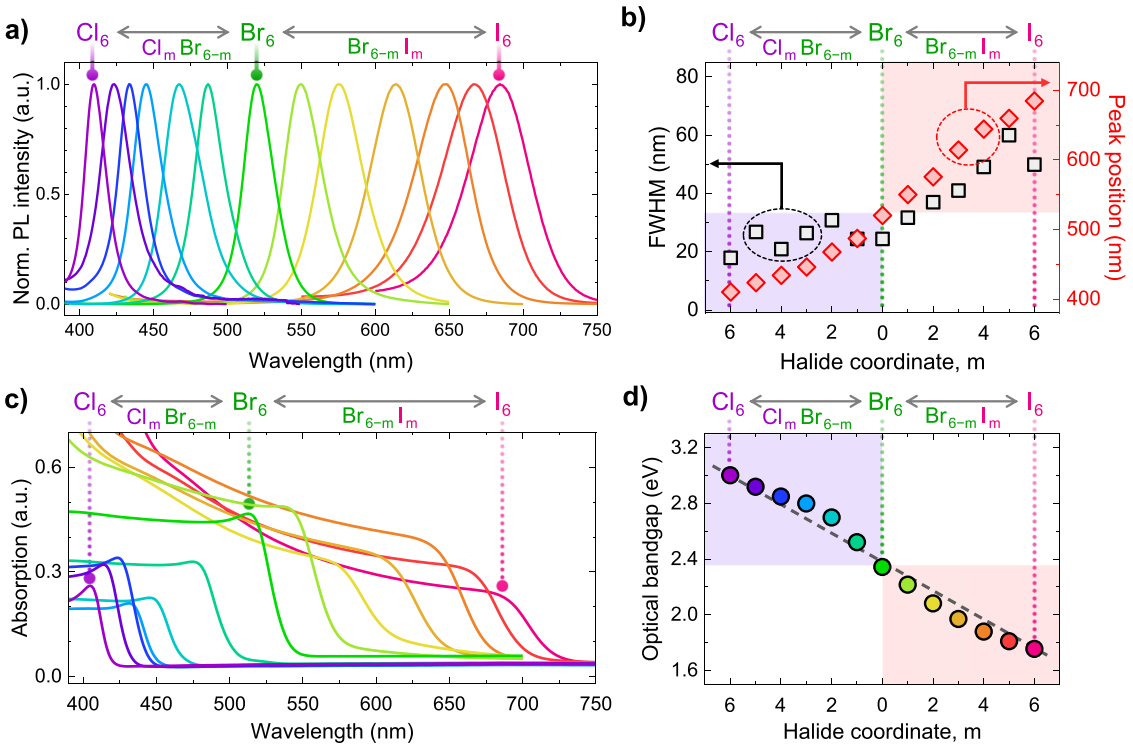

Figure 3. (a) PL spectra and (b) FWHM and peak positions of the PL spectra for the synthesized powder samples under excitation wavelengths of 365 and 400 nm, respectively. (c) Absorption spectra within the visible light range (400−750 nm). (d) Optical band gap of the emissive powder samples calculated using the Tauc plot method.

incorporate local halide segregations at a microscopic level (e.g., $[CsCl_3Br_5]^{7-}$ environment is locally rich in Br) as part of its feature, which would naturally lead to a broadening of PL emissions (vide infra). Since the variation of Cs(1) shifts with intermediate compositions is expected to be linear within the Cs(1) NMR shifts of isostructural end-members Cs_4PbCl_6 (187 ppm), Cs_4PbBr_6 (227 ppm), and Cs_4PbI_6 (265 ppm), this would therefore result in significant broadening of the mixed-halide peaks occupying the whole range of shifts between that of monohalide samples. This fact is in stark contrast to the single-halide case, where only a single such local coordination environment, $[CsX_8]^{7-}$, is possible, thus sharp Cs(1) resonances are observed for each site. Note that quadrupolar effects, which may also provide the source of such peak broadening upon halide substitution, are expected to be rather minor from the comparison of individual spectra taken at two different magnetic fields (14.1 and 11.7 T; see Figure S3 in the Supporting Information). An identical conclusion may be made from the observation of the Cs(2) peaks, which shows a similar broadening upon halide mixing (but with higher overall chemical shifts). Thus, the loss in resolution arising from these broad Cs resonances provides direct evidence of Cl/Br and Br/I halide mixing on an atomistic level, a result consistent with the changes in the PXRD lattice parameters. This result is also consistent with the gradual evolution of the Pb−X Raman stretching mode (A_{1g}) depending on the halide ratio (see the Supporting Information, Figure S4), suggesting the coexistence of Cl/Br atoms or Br/I atoms in the lattice structure of the mixed-halide 0D perovskites.

3.2. Evolution of Optical Properties upon Halide Substitution. After confirming the viability of the MCS approach for synthesizing 0D perovskite powder samples with mixed-halide compositions, we now turn our attention to the optical characterization of these samples, starting with the PL spectra (Figure 3a). Upon tuning the halide composition from Cs_4PbCl_6 to Cs_4PbI_6, the emission peak wavelength is shown to span across the entire visible spectrum from 410 to 690 nm. This result demonstrates the feasibility of providing the entire visible spectrum by simply changing the halide ratio of 0D perovskites, and it is consistent with the results from previous studies.[10] Visible emission of these mixed-halide 0D perovskites can be attributed to the 3D perovskite nanocrystals embedded in the 0D perovskite matrix, which is discussed in detail later. Two main properties of each PL spectrum, i.e., FWHM and peak position, are also summarized in Figure 3b. The samples exhibit a narrow FWHM of 17−60 nm (see the black squares in Figure 3b). The mixed-halide samples show broader FWHM than monohalide samples due to the presence of multiple halide environments in mixed-halide samples as discussed above (see the Supporting Information, Figure S5).

Absorption measurements were also performed on the samples to investigate the origin of the PL emission in the visible spectrum range (Figures 3c and S6 in the Supporting Information). As viewed in the same spectral range from the PL spectra in Figure 3a, the absorption onset position for each sample is evident within the visible spectrum range. Finally, Figure 3d shows the extracted optical band gaps of each sample acquired through the Tauc plot method.[41] The band gaps increase from 1.75 to 3.00 eV with increasing Br/I and Cl/Br ratios. Furthermore, Figure 3d shows a crucial trend when one tries to synthesize a target mixed-halide 0D perovskite sample with a specific optical band gap through MCS which allows a fine tuning of different halide compositions by modifying the molar ratio of solid-state precursors. The PLQE values of the synthesized powder samples are reported in Section 2.2 of the Supporting Information.

https://doi.org/10.1021/acs.chemmater.3c00833
Chem. Mater. XXXX, XXX, XXX−XXX

Since such a stairlike band-to-band absorption trend typically originates from the conventional 3D perovskite phases that are significantly more emissive in the nanocrystalline form, we

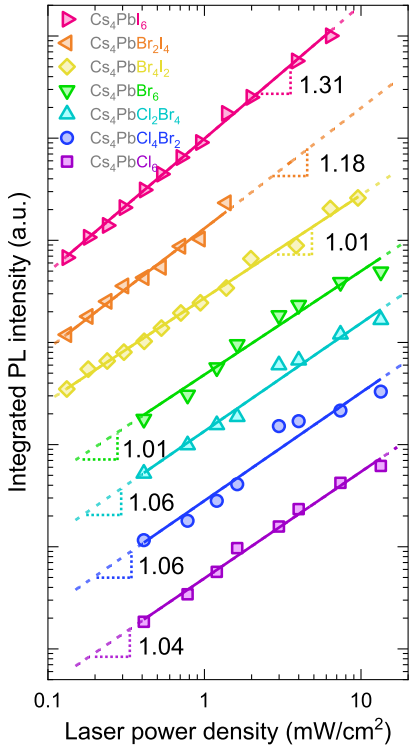

Figure 4. Integrated PL intensities as a function of excitation laser power density for $Cs_4PbCl_mBr_{6-m}$ (m = 6, 4, 2, 0) samples excited by a 405 nm laser and $Cs_4PbBr_{6-m}I_m$ (m = 6, 4, 2) samples excited by a 532 nm laser. For clariy, the integrated PL intensity lines were shifted along the y-axis.

hypothesized that the visible emission of the 0D perovskites originates from their inclusion of nanosized 3D perovskite crystals. In order to support this hypothesis, the trend of the integrated PL intensity was examined as a function of the excitation source power to provide an analysis of the visible light emission through identifying the type of recombination process (Figure 4). On the basis of different recombination mechanisms, there are several possible scenarios that can explain the origin of visible light emission in 0D perovskites: (1) defect states in 0D perovskite band gaps,[34] (2) self-trapped exciton formed by structural distortion,[42,43] and (3) free exciton in 3D perovskite nanoparticles embedded in the 0D perovskite.[19,44] In this regard, it is known that the intensity of PL is proportional to P^{γ}, where P is the power of the excitation laser source and γ is an exponent coefficient between 0 and 2. When γ lies between 1 and 2 ($1 < \gamma < 2$), the emission is attributed to the excitonic recombination. On the other hand, when γ gets smaller than 1 ($\gamma < 1$), the emission is attributed to donor−acceptor pair transition and free-to-bound transition which is radiative recombination of a free electron and a neutral acceptor or a free hole and a neutral donor.[45]

Here, we use a process of elimination to identify the origin of PL emission with 3D perovskite nanoparticles as visible light emitters embedded in the 0D perovskite. First, Figure 4 shows that all of the γ values for the mixed-halide perovskite samples are larger than 1, indicating that the PL originates from a recombination process of excitons (see Section 2.3 in the Supporting Information). This observation excludes the possibility of the first scenario mentioned above (i.e., transition within defect states in the 0D perovskite band gaps). Moreover, according to the visible emission spectra and the narrow FWHM (17−60 nm) of mixed-halide 0D perovskites in Figure 3b, the PL emission does not originate from a self-trapped exciton that must accompany PL in the UV region and broad FWHM (>100 nm),[46,47] thereby excluding the second scenario. The fact that the visible light most likely originates from free excitonic recombination supports the hypothesis that visible emission is attributed to 3D perovskite nanocrystals embedded in the 0D perovskite. The detailed excitonic recombination corresponding to the 0D or 3D perovskites is examined through the contour plots of the PL intensity as a function of excitation and emission wavelengths (see the Supporting Information, Figure S10). Moreover, the PL excitation (PLE) spectra show further evidence of the 3D@0D perovskite structure (see the Supporting Information, Figure S11). A rough estimate of <1 wt % can be made of the upper limit of 3D concentration in our 0D perovskite sample (see Section 2.5 in the Supporting Information).

The case of Cs_4PbI_6, however, needs further attention since two different polymorphs of $CsPbI_3$ are known to exist: the γ-$CsPbI_3$ perovskite phase that emits narrow red light through free excitonic recombination and the δ-$CsPbI_3$ nonperovskite phase that renders weak broad emission due to self-trapped excitons (see the Supporting Information, Figure S13). γ-$CsPbI_3$ is thermodynamically unstable under ambient environments and spontaneously transforms into a δ-phase nonperovskite phase, thus losing its optical properties.[48] Even though only the weakly emissive δ-$CsPbI_3$ phase is detected in our ssNMR spectrum of the Cs_4PbI_6 powder (Figure 2c), the intense red emission with narrow FWHM arising from this sample strongly indicates the presence of thermodynamically unstable γ-$CsPbI_3$, a red emitter, under ambient conditions. We speculate that this stabilization of perovskite-type $CsPbI_3$ may originate from a "pinning" effect induced by lattice matching, which means that the interfacial bonding between 3D and 0D perovskites at well-matched lattice interfaces may inhibit such phase transitions.[16,23,49] Since the lattice constants of γ-$CsPbI_3$ are smaller than those of δ-$CsPbI_3$, a certain amount of space is required for the unit cell volume change. In this regard, Cs_4PbI_6 surrounding γ-$CsPbI_3$ constrains the space for phase transition, resulting in preservation of γ-$CsPbI_3$.[49] Additional stability results of the perovskite powder samples are provided in Section 2.7 of the Supporting Information.

3.3. Transferring the Tunable Emission of the Powder Samples to Films through Flash Evaporation. For many optoelectronic applications, perovskite materials need to be fabricated into films, rather than the powder form. Conventionally, spin-coating has been widely utilized as a deposition method due to its low cost and readily accessible process.[50] However, this solution-based process has several issues with regard to producing high-quality perovskite films because of the poor solubility of cesium halides in common solvents and the difficulties of large and uniform deposition, so vacuum deposition has been introduced as an alternative method. Unreacted powder precursors (e.g., CsX and PbX_2) can be deposited either simultaneously (coevaporation)[28] or sequentially (2-step evaporation),[51] but it is challenging to produce perovskite films with the intended stoichiometric ratio between the elements because of different vaporization temperatures of the precursors. In order to avoid the aforementioned issues, we

https://doi.org/10.1021/acs.chemmater.3c00833
Chem. Mater. XXXX, XXX, XXX−XXX

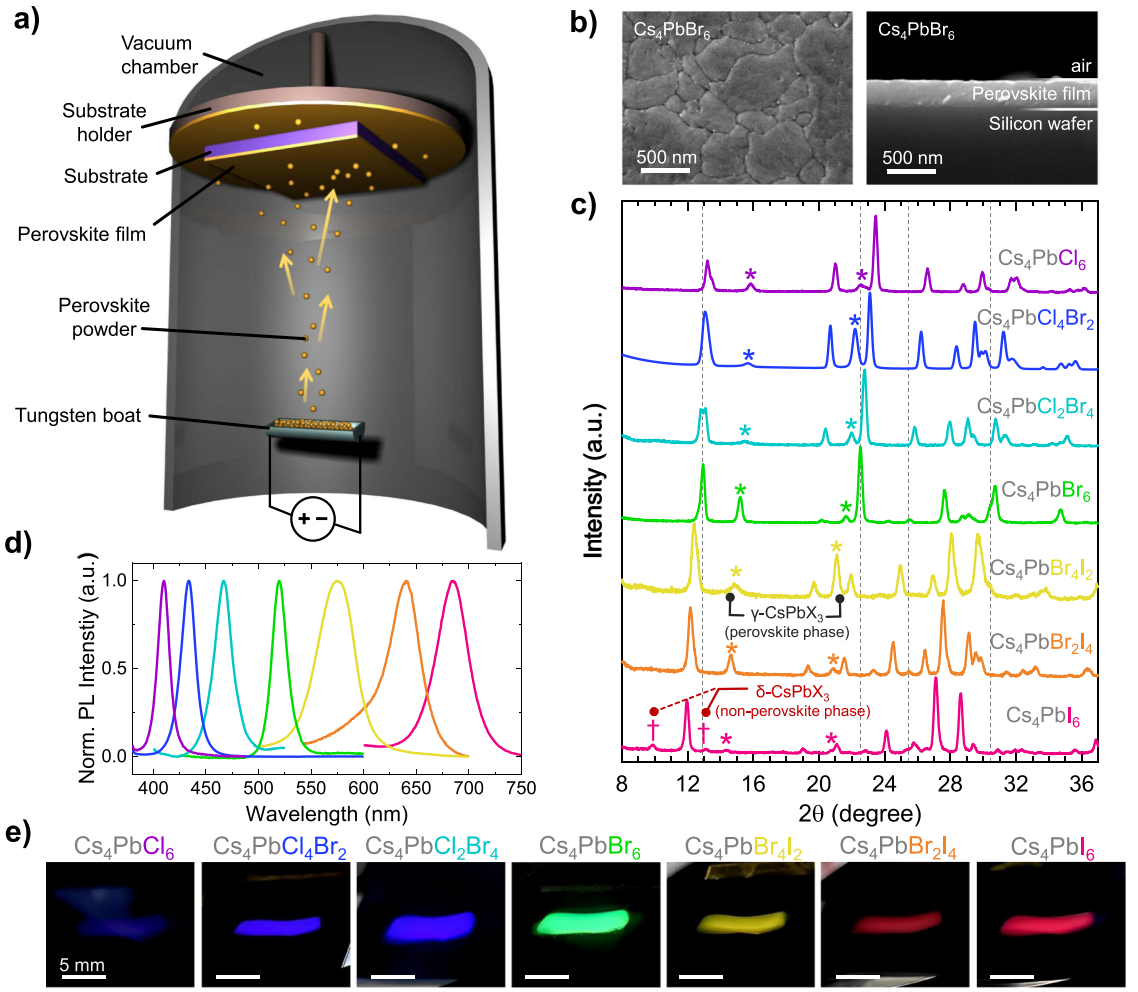

Figure 5. (a) Schematic image of single-source vacuum deposition to prepare perovskite films with mechanochemically synthesized perovskite powder samples. (b) Top view (left) and cross-section view (right) FE-SEM images of the Cs_4PbBr_6 film. (c) HRXRD characterization of the perovskite films after an annealing process. Two different types of $CsPbX_3$ inclusions (perovskite phase and nonperovskite phase) are marked with asterisks (*) and daggers (†), respectively. (d) PL spectra of the $Cs_4PbCl_mBr_{6-m}$ (m = 6, 4, 2, 0) and $Cs_4PbBr_{6-m}I_m$ (m = 6, 4, 2) films under excitation wavelengths of 365 nm and 400 nm, respectively. (e) Restored images from the original photographs of the samples under UV irradiation without adjusting the color.

employed a single-source vacuum deposition (SSVD) technique for film deposition as it enables the direct usage of mechanochemically synthesized products bypassing the solubility issues of the spin-coating technique and also allows uniform large-area deposition.[52,53] Especially, presynthesized 0D perovskite powder samples are used as a source of deposition, which avoids the problem of failing to produce the desired films when using unreacted mixed precursor sources. Figure 5a illustrates our SSVD setup, where a heating current (140 A) is applied to a tungsten boat containing the as-synthesized powder samples. The powder samples are then evaporated and sequentially deposited onto the substrate in vacuum at 5×10^{-6} Torr. Then, the films were annealed at 150 °C for 5 min after the deposition. The representative FE-SEM images of the deposited Cs_4PbBr_6 film, as shown in Figure 5b, clearly demonstrate the uniform surface quality with a thickness of ~250 nm (see the Supporting Information, Figure S17).

In order to validate the transferability of the 0D perovskite structures of the source powder to the deposited films, we examined the X-ray diffraction (XRD) patterns of the deposited films (Figure 5c). The resulting data shows identical diffraction patterns corresponding to those of 0D perovskite powder samples (see the Supporting Information, Figure S18), therefore confirming the successful deposition of 0D perovskite on the substrates. Overall, a gradual shift of 2θ values to lower angles with increasing halide sizes is observed, also similar to that of Figure 2a for powder samples.

However, reflections originating from the phases other than the 0D perovskite structure are also observed in the deposited films (see the asterisks and daggers in Figures 5c and S18 in the Supporting Information), in contrast to the PXRD data. In particular, the asterisks in Figure 5c represent the existence of γ-phase 3D perovskite structure responsible for the visible light emission in the form of nanoparticles in our study. Note that for the samples rich in iodine (i.e., $Cs_4PbBr_2I_4$ and Cs_4PbI_6 samples), a δ-$CsPbX_3$ phase (nonperovskite) was also detected on the as-deposited film, which is shown to vanish upon thermal annealing (see the Supporting Information, Figure S18). Since $CsPbI_3$ is known to readily undergo a phase transition from the emissive γ-phase to nonemissive δ-phase even under an ambient room-temperature environment due to a small difference in the enthalpy of formation between the two phases,[27] this result is rather surprising and indicates a potential stabilization route of the γ-$CsPbX_3$ phase within the 0D perovskite matrix upon thermal annealing. Here, we speculate that the postannealing process subsequently transforms the undesired δ-phase non-

https://doi.org/10.1021/acs.chemmater.3c00833
Chem. Mater. XXXX, XXX, XXX−XXX

perovskites into γ-phase 3D perovskites within the 0D perovskite matrix; such a 0D perovskite matrix may stabilize the γ-phase perovskites through the interfacial "pinning" effect, as discussed above.[49]

In analogy with the characterization of powder samples, we examined the PL properties of the deposited films. Figure 5e shows optical images of the deposited films under a 400 nm light source. From the Cs_4PbCl_6 film to the Cs_4PbI_6 film (left to right image of Figure 5e), a light emission spanning the visible spectrum (from purple to red) can be demonstrated. Figure 5d shows the PL spectra measured for each film which have identical peak positions to those of the powder samples (see the Supporting Information, Figure S19). The Cs_4PbCl_6 film before annealing has nearly the same PL peak wavelength as that of the powder sample. On the other hand, the PL peak wavelengths of the as-deposited films from $Cs_4PbCl_4Br_2$ to Cs_4PbBr_6 are slightly different from those of the powder samples (the difference being approx. 5.0−7.5 nm) with a slightly larger difference observed in the $Cs_4PbBr_4I_2$ films (18 nm) and even larger differences observed in the $Cs_4PbBr_2I_4$ and Cs_4PbI_6 films (80−100 nm) (see Figure S20 and Table S3 in the Supporting Information). Here, the postannealing process with the same condition mentioned above also plays an important role in matching the PL peak wavelengths of the films with those of the powder samples. The role of the postannealing process in tuning the PL peak wavelengths of the films can be potentially attributed to the following effects: (1) readjusting the 3D perovskite nanoparticle size (all halides),[54] (2) redistributing the Br- and I-rich domains in the 3D perovskites,[55,56] and (3) converting the δ-phase nonperovskite iodides into γ-phase,[57] which are demonstrated through our comparative XRD results (see the Supporting Information, Section 3.2).

Overall, by employing the SSVD method accompanied with the postannealing process, we successfully transcribed the mechanochemically synthesized 0D perovskite powder samples into films while retaining their optical properties. Application of these films includes color-conversion filters for LEDs (UV to visible lights), which is demonstrated in Section 3.4 in the Supporting Information.

4. CONCLUSIONS

In summary, we demonstrated the successful synthesis of nominal 0D mixed-halide perovskite powder samples through mechanochemical synthesis. These samples are likely to form 3D@0D perovskites that are visible light emitters, where the emission wavelength can be tuned by modifying the overall halide ratio of the samples ($Cs_4PbCl_mBr_{6-m}$ and $Cs_4PbBr_{6-m}I_m$, where m is an integer from 0 to 6). The absorption and excitation power-dependent PL spectra indicated that the visible light emission in the samples likely originates from the excitonic recombination in the 3D perovskite nanoparticles encapsulated inside the 0D perovskite matrix. We also fabricated perovskite films using the as-synthesized perovskite powder samples and demonstrated that both the 0D mixed-halide perovskite structure and optical properties can be well retained during film deposition via single-source flash evaporation. Overall, this work demonstrates the possibility of the nanoscale structural control of mixed-composition perovskites via a simple solid-state synthesis, as well as incorporation of perovskite phases with mixed dimensions for efficient light emission. The facile synthesis method of bulk perovskites demonstrated in this work and their utilization as a source for thin-film deposition are highly relevant for developing perovskite-based optoelectronic devices.

■ ASSOCIATED CONTENT

Supporting Information

The Supporting Information is available free of charge at https://pubs.acs.org/doi/10.1021/acs.chemmater.3c00833.

Details for PXRD, SEM, ssNMR, and Raman spectra characterization of the powder samples; absorption, PLQE, contour plots of PL intensity, and PLE analysis; structural and optical stability data; XRD and PL spectra of perovskite films before and after annealing; and color-conversion layer of perovskite films (PDF)

■ AUTHOR INFORMATION

Corresponding Authors

Jeongjae Lee − *School of Earth and Environmental Sciences, Seoul National University, Seoul 08826, Korea;* orcid.org/0000-0003-4294-4993; Email: jl635@snu.ac.kr

Keehoon Kang − *Department of Materials Science and Engineering, Research Institute of Advanced Materials, and Institute of Applied Physics, Seoul National University, Seoul 08826, Korea*; Email: keehoon.kang@snu.ac.kr

Takhee Lee − *Department of Physics and Astronomy, Seoul National University, Seoul 08826, Korea; Institute of Applied Physics, Seoul National University, Seoul 08826, Korea;* orcid.org/0000-0001-5988-5219; Email: tlee@snu.ac.kr

Authors

Hyungbin Lim − *Department of Physics and Astronomy, Seoul National University, Seoul 08826, Korea*

Kyeong-Yoon Baek − *Department of Physics and Astronomy, Seoul National University, Seoul 08826, Korea;* Present Address: Department of Physics, Harvard University, Cambridge, Massachusetts 02138, USA

Jae Il Kim − *Department of Materials Science and Engineering and Research Institute of Advanced Materials, Seoul National University, Seoul 08826, Korea*

Jonghoon Lee − *Department of Physics and Astronomy, Seoul National University, Seoul 08826, Korea*

Jaeyoung Kim − *Department of Physics and Astronomy, Seoul National University, Seoul 08826, Korea*

Heebeom Ahn − *Department of Physics and Astronomy, Seoul National University, Seoul 08826, Korea*

Hyeonmin Choi − *Department of Materials Science and Engineering, Seoul National University, Seoul 08826, Korea*

Seung-Je Woo − *Department of Materials Science and Engineering, Seoul National University, Seoul 08826, Korea*

Sung Keun Lee − *School of Earth and Environmental Sciences and Institute of Applied Physics, Seoul National University, Seoul 08826, Korea;* orcid.org/0000-0002-3149-3421

Tae-Woo Lee − *Department of Materials Science and Engineering, Research Institute of Advanced Materials, and School of Chemical and Biological Engineering, Institute of Engineering Research, Soft Foundry, Seoul National University, Seoul 08826, Korea;* orcid.org/0000-0002-6449-6725

Complete contact information is available at: https://pubs.acs.org/10.1021/acs.chemmater.3c00833

Author Contributions

[▽]H. L. and K.-Y. B. contributed equally to this work.

https://doi.org/10.1021/acs.chemmater.3c00833
Chem. Mater. XXXX, XXX, XXX−XXX

Notes

The authors declare no competing financial interest.

■ ACKNOWLEDGMENTS

The authors appreciate the financial support of the National Research Foundation of Korea (NRF) grant (No. 2021R1A2C3004783, No. 2021R1C1C1010266, No. 2016R1A3B1908431, and No. 2020R1A3B2079815), the BrainLink program (No. 2022H1D3A3A01077343), and the NanoMaterial Technology Development Program grant (No. 2021M3H4A1A02049651) through NRF funded by the Ministry of Science and ICT (MSIT) of Korea, and the industry−university cooperation program by Samsung Electronics Co., Ltd. (IO201211-08047-01). Jeongjae L. was supported by the NRF grant funded by the MSIT of Korea (No. 2019R1A6A1A10073437). The authors acknowledge support from the National Center for Inter-University Research Facilities (NCIRF) at Seoul National University for PXRD, ssNMR measurements, and FE-SEM observations, and Research Institute of Advanced Materials (RIAM) at Seoul National University for absorption measurements. 14.1 T and 11.7 T NMR data were acquired at KBSI Seoul Western Center and NCIRF, respectively. The authors thank Dokyung Kim, Dr Young Joo Lee, and Dr Yoon-Joo Ko for assisting with NMR measurements.

■ REFERENCES

(1) Tan, Z.-K.; Moghaddam, R. S.; Lai, M. L.; Docampo, P.; Higler, R.; Deschler, F.; Price, M.; Sadhanala, A.; Pazos, L. M.; Credgington, D.; et al. Bright light-emitting diodes based on organometal halide perovskite. *Nat. Nanotechnol.* **2014**, *9*, 687−692.

(2) Cho, H.; Jeong, S.-H.; Park, M.-H.; Kim, Y.-H.; Wolf, C.; Lee, C.-L.; Heo, J. H.; Sadhanala, A.; Myoung, N.; Yoo, S.; et al. Overcoming the electroluminescence efficiency limitations of perovskite light-emitting diodes. *Science* **2015**, *350*, 1222−1225.

(3) Zhao, B.; Bai, S.; Kim, V.; Lamboll, R.; Shivanna, R.; Auras, F.; Richter, J. M.; Yang, L.; Dai, L.; Alsari, M.; et al. High-efficiency perovskite−polymer bulk heterostructure light-emitting diodes. *Nat. Photonics* **2018**, *12*, 783−789.

(4) Hassan, Y.; Park, J. H.; Crawford, M. L.; Sadhanala, A.; Lee, J.; Sadighian, J. C.; Mosconi, E.; Shivanna, R.; Radicchi, E.; Jeong, M.; et al. Ligand-engineered bandgap stability in mixed-halide perovskite LEDs. *Nature* **2021**, *591*, 72−77.

(5) Jeon, N. J.; Na, H.; Jung, E. H.; Yang, T.-Y.; Lee, Y. G.; Kim, G.; Shin, H.-W.; Il Seok, S.; Lee, J.; Seo, J. A fluorene-terminated hole-transporting material for highly efficient and stable perovskite solar cells. *Nat. Energy* **2018**, *3*, 682−689.

(6) Green, M. A.; Ho-Baillie, A.; Snaith, H. J. The emergence of perovskite solar cells. *Nat. Photonics* **2014**, *8*, 506−514.

(7) Jeong, J.; Kim, M.; Seo, J.; Lu, H.; Ahlawat, P.; Mishra, A.; Yang, Y.; Hope, M. A.; Eickemeyer, F. T.; Kim, M.; et al. Pseudo-halide anion engineering for α-$FAPbI_3$ perovskite solar cells. *Nature* **2021**, *592*, 381−385.

(8) Niu, T.; Lu, J.; Munir, R.; Li, J.; Barrit, D.; Zhang, X.; Hu, H.; Yang, Z.; Amassian, A.; Zhao, K.; Liu, S. F. Stable High-Performance Perovskite Solar Cells via Grain Boundary Passivation. *Adv. Mater.* **2018**, *30*, No. 1706576.

(9) Dou, L.; Yang, Y.; You, J.; Hong, Z.; Chang, W.-H.; Li, G.; Yang, Y. Solution-processed hybrid perovskite photodetectors with high detectivity. *Nat. Commun.* **2014**, *5*, No. 5404.

(10) Protesescu, L.; Yakunin, S.; Bodnarchuk, M. I.; Krieg, F.; Caputo, R.; Hendon, C. H.; Yang, R. X.; Walsh, A.; Kovalenko, M. V. Nanocrystals of Cesium Lead Halide Perovskites ($CsPbX_3$, X = Cl, Br, and I): Novel Optoelectronic Materials Showing Bright Emission with Wide Color Gamut. *Nano Lett.* **2015**, *15*, 3692−3696.

(11) Akkerman, Q. A.; D'Innocenzo, V.; Accornero, S.; Scarpellini, A.; Petrozza, A.; Prato, M.; Manna, L. Tuning the Optical Properties of Cesium Lead Halide Perovskite Nanocrystals by Anion Exchange Reactions. *J. Am. Chem. Soc.* **2015**, *137*, 10276−10281.

(12) Chen, D.; Li, J.; Chen, X.; Chen, J.; Zhong, J. Grinding Synthesis of $APbX_3$ (A = MA, FA, Cs; X = Cl, Br, I) Perovskite Nanocrystals. *ACS Appl. Mater. Interfaces* **2019**, *11*, 10059−10067.

(13) Butler, K. T.; Frost, J. M.; Walsh, A. Band alignment of the hybrid halide perovskites $CH_3NH_3PbCl_3$, $CH_3NH_3PbBr_3$ and $CH_3NH_3PbI_3$. *Mater. Horizons* **2015**, *2*, 228−231.

(14) Saidaminov, M. I.; Mohammed, O. F.; Bakr, O. M. Low-Dimensional-Networked Metal Halide Perovskites: The Next Big Thing. *ACS Energy Lett.* **2017**, *2*, 889−896.

(15) Akkerman, Q. A.; Rainò, G.; Kovalenko, M. V.; Manna, L. Genesis, challenges and opportunities for colloidal lead halide perovskite nanocrystals. *Nat. Mater.* **2018**, *17*, 394−405.

(16) Hou, J.; Chen, P.; Shukla, A.; Krajnc, A.; Wang, T.; Li, X.; Doasa, R.; Tizei Luiz, H. G.; Chan, B.; Johnstone, D. N.; et al. Liquid-phase sintering of lead halide perovskites and metal-organic framework glasses. *Science* **2021**, *374*, 621−625.

(17) Quan, L. N.; Quintero-Bermudez, R.; Voznyy, O.; Walters, G.; Jain, A.; Fan, J. Z.; Zheng, X.; Yang, Z.; Sargent, E. H. Highly Emissive Green Perovskite Nanocrystals in a Solid State Crystalline Matrix. *Adv. Mater.* **2017**, *29*, No. 1605945.

(18) Chen, Y.-M.; Zhou, Y.; Zhao, Q.; Zhang, J.-Y.; Ma, J.-P.; Xuan, T.-T.; Guo, S.-Q.; Yong, Z.-J.; Wang, J.; Kuroiwa, Y.; et al. Cs_4PbBr_6/$CsPbBr_3$ Perovskite Composites with Near-Unity Luminescence Quantum Yield: Large-Scale Synthesis, Luminescence and Formation Mechanism, and White Light-Emitting Diode Application. *ACS Appl. Mater. Interfaces* **2018**, *10*, 15905−15912.

(19) Saidaminov, M. I.; Almutlaq, J.; Sarmah, S.; Dursun, I.; Zhumekenov, A. A.; Begum, R.; Pan, J.; Cho, N.; Mohammed, O. F.; Bakr, O. M. Pure Cs_4PbBr_6: Highly Luminescent Zero-Dimensional Perovskite Solids. *ACS Energy Lett.* **2016**, *1*, 840−845.

(20) Cao, F.; Yu, D.; Xu, X.; Han, Z.; Zeng, H. $CsPbBr_3$@Cs_4PbBr_6 Emitter-in-Host Composite: Fluorescence Origin and Interphase Energy Transfer. *J. Phys. Chem. C* **2021**, *125*, 3−19.

(21) Qin, Z.; Dai, S.; Hadjiev, V. G.; Wang, C.; Xie, L.; Ni, Y.; Wu, C.; Yang, G.; Chen, S.; Deng, L.; et al. Revealing the Origin of Luminescence Center in 0D Cs_4PbBr_6 Perovskite. *Chem. Mater.* **2019**, *31*, 9098−9104.

(22) Baek, K.-Y.; Lee, W.; Lee, J.; Kim, J.; Ahn, H.; Kim, J. I.; Kim, J.; Lim, H.; Shin, J.; Ko, Y.-J.; et al. Mechanochemistry-driven engineering of 0D/3D heterostructure for designing highly luminescent Cs−Pb−Br perovskites. *Nat. Commun.* **2022**, *13*, No. 4263.

(23) Grandhi, G. K.; Viswanath, N. S. M.; In, J. H.; Cho, H. B.; Im, W. B. Robust, Brighter Red Emission from $CsPbI_3$ Perovskite Nanocrystals via Endotaxial Protection. *J. Phys. Chem. Lett.* **2020**, *11*, 3699−3704.

(24) Arunkumar, P.; Cho, H. B.; Gil, K. H.; Unithrattil, S.; Kim, Y. H.; Bin Im, W. Probing molecule-like isolated octahedra via phase stabilization of zero-dimensional cesium lead halide nanocrystals. *Nat. Commun.* **2018**, *9*, No. 4691.

(25) Karmakar, A.; Askar, A. M.; Bernard, G. M.; Terskikh, V. V.; Ha, M.; Patel, S.; Shankar, K.; Michaelis, V. K. Mechanochemical Synthesis of Methylammonium Lead Mixed−Halide Perovskites: Unraveling the Solid-Solution Behavior Using Solid-State NMR. *Chem. Mater.* **2018**, *30*, 2309−2321.

(26) Askar, A. M.; Karmakar, A.; Bernard, G. M.; Ha, M.; Terskikh, V. V.; Wiltshire, B. D.; Patel, S.; Fleet, J.; Shankar, K.; Michaelis, V. K. Composition-Tunable Formamidinium Lead Mixed Halide Perovskites via Solvent-Free Mechanochemical Synthesis: Decoding the Pb Environments Using Solid-State NMR Spectroscopy. *J. Phys. Chem. Lett.* **2018**, *9*, 2671−2677.

(27) Wu, X.; Zhou, Q.; Wu, H.; Du, X.; Niu, G.; Liang, G.; Hu, Q.; Xiao, J. $Cs_4PbBr_{6-x}Cl_x$ Single Crystals with Tunable Emission for X-ray Detection and Imaging. *J. Phys. Chem. C* **2021**, 26619−26626.

(28) Wang, X.; Ling, Y.; Lian, X.; Xin, Y.; Dhungana, K. B.; Perez-Orive, F.; Knox, J.; Chen, Z.; Zhou, Y.; Beery, D.; et al. Suppressed

https://doi.org/10.1021/acs.chemmater.3c00833
Chem. Mater. XXXX, XXX, XXX−XXX

phase separation of mixed-halide perovskites confined in endotaxial matrices. *Nat. Commun.* **2019**, *10*, No. 695.
(29) Palazon, F.; El Ajjouri, Y.; Bolink, H. J. Making by Grinding: Mechanochemistry Boosts the Development of Halide Perovskites and Other Multinary Metal Halides. *Adv. Energy Mater.* **2020**, *10*, No. 1902499.
(30) Palazon, F.; El Ajjouri, Y.; Sebastia-Luna, P.; Lauciello, S.; Manna, L.; Bolink, H. J. Mechanochemical synthesis of inorganic halide perovskites: evolution of phase-purity, morphology, and photoluminescence. *J. Mater. Chem. C* **2019**, *7*, 11406−11410.
(31) Toby, B. H.; Von Dreele, R. B. GSAS-II: the genesis of a modern open-source all purpose crystallography software package. *J. Appl. Crystallogr.* **2013**, *46*, 544−549.
(32) Akkerman, Q. A.; Abdelhady, A. L.; Manna, L. Zero-Dimensional Cesium Lead Halides: History, Properties, and Challenges. *J. Phys. Chem. Lett.* **2018**, *9*, 2326−2337.
(33) Cha, J.-H.; Lee, H.-J.; Kim, S. H.; Ko, K. C.; Suh, B. J.; Han, O. H.; Jung, D.-Y. Superparamagnetism of Green Emissive Cs_4PbBr_6 Zero-Dimensional Perovskite Crystals. *ACS Energy Lett.* **2020**, *5*, 2208−2216.
(34) De Bastiani, M.; Dursun, I.; Zhang, Y.; Alshankiti, B. A.; Miao, X.-H.; Yin, J.; Yengel, E.; Alarousu, E.; Turedi, B.; Almutlaq, J. M.; et al. Inside Perovskites: Quantum Luminescence from Bulk Cs_4PbBr_6 Single Crystals. *Chem. Mater.* **2017**, *29*, 7108−7113.
(35) Møller, C. K.; selskab, K. D. V. *On the Structure of Cæsium Hexahalogeno-plumbates (II)*; Munksgaard: København Denmark, 1960.
(36) Noh, J. H.; Im, S. H.; Heo, J. H.; Mandal, T. N.; Seok, S. I. Chemical Management for Colorful, Efficient, and Stable Inorganic−Organic Hybrid Nanostructured Solar Cells. *Nano Lett.* **2013**, *13*, 1764−1769.
(37) Shannon, R. D. Revised effective ionic radii and systematic studies of interatomic distances in halides and chalcogenides. *Acta Crystallogr., Sect. A* **1976**, *32*, 751−767.
(38) Haase, A. R.; Kerber, M. A.; Kessler, D.; Kronenbitter, J.; Krüger, H.; Lutz, O.; Müller, M.; Nolle, A. Nuclear Magnetic Shielding and Quadrupole Coupling of ^{133}Cs in Cesium Salt Powders. *Z. Naturforsch., A* **1977**, *32*, 952−956.
(39) Slichter, C. P. *Principles of Magnetic Resonance*; Springer Berlin Heidelberg, 1996.
(40) Karmakar, A.; Dodd, M. S.; Zhang, X.; Oakley, M. S.; Klobukowski, M.; Michaelis, V. K. Mechanochemical synthesis of 0D and 3D cesium lead mixed halide perovskites. *Chem. Commun.* **2019**, *55*, 5079−5082.
(41) Makuła, P.; Pacia, M.; Macyk, W. How To Correctly Determine the Band Gap Energy of Modified Semiconductor Photocatalysts Based on UV−Vis Spectra. *J. Phys. Chem. Lett.* **2018**, *9*, 6814−6817.
(42) Kang, B.; Biswas, K. Exploring Polaronic, Excitonic Structures and Luminescence in $Cs_4PbBr_6/CsPbBr_3$. *J. Phys. Chem. Lett.* **2018**, *9*, 830−836.
(43) Yin, J.; Zhang, Y.; Bruno, A.; Soci, C.; Bakr, O. M.; Brédas, J.-L.; Mohammed, O. F. Intrinsic Lead Ion Emissions in Zero-Dimensional Cs_4PbBr_6 Nanocrystals. *ACS Energy Lett.* **2017**, *2*, 2805−2811.
(44) Baranowski, M.; Plochocka, P. Excitons in Metal-Halide Perovskites. *Adv. Energy Mater.* **2020**, *10*, No. 1903659.
(45) Schmidt, T.; Lischka, K.; Zulehner, W. Excitation-power dependence of the near-band-edge photoluminescence of semiconductors. *Phys. Rev. B* **1992**, *45*, 8989−8994.
(46) Bhaumik, S.; Bruno, A.; Mhaisalkar, S. Broadband emission from zero-dimensional Cs_4PbI_6 perovskite nanocrystals. *RSC Adv.* **2020**, *10*, 13431−13436.
(47) Li, S.; Luo, J.; Liu, J.; Tang, J. Self-Trapped Excitons in All-Inorganic Halide Perovskites: Fundamentals, Status, and Potential Applications. *J. Phys. Chem. Lett.* **2019**, *10*, 1999−2007.
(48) Sutton, R. J.; Filip, M. R.; Haghighirad, A. A.; Sakai, N.; Wenger, B.; Giustino, F.; Snaith, H. J. Cubic or Orthorhombic? Revealing the Crystal Structure of Metastable Black-Phase $CsPbI_3$ by Theory and Experiment. *ACS Energy Lett.* **2018**, *3*, 1787−1794.
(49) Bai, F.; Zhang, J.; Yuan, Y.; Liu, H.; Li, X.; Chueh, C.-C.; Yan, H.; Zhu, Z.; Jen, A. K. Y. A 0D/3D Heterostructured All-Inorganic Halide Perovskite Solar Cell with High Performance and Enhanced Phase Stability. *Adv. Mater.* **2019**, *31*, No. 1904735.
(50) Xu, J.; Huang, W.; Li, P.; Onken, D. R.; Dun, C.; Guo, Y.; Ucer, K. B.; Lu, C.; Wang, H.; Geyer, S. M.; et al. Imbedded Nanocrystals of $CsPbBr_3$ in Cs_4PbBr_6: Kinetics, Enhanced Oscillator Strength, and Application in Light-Emitting Diodes. *Adv. Mater.* **2017**, *29*, No. 1703703.
(51) Shin, M.; Nam, S.-W.; Sadhanala, A.; Shivanna, R.; Anaya, M.; Jiménez-Solano, A.; Yoon, H.; Jeon, S.; Stranks, S. D.; Hoye, R. L. Z.; Shin, B. Understanding the Origin of Ultrasharp Sub-bandgap Luminescence from Zero-Dimensional Inorganic Perovskite Cs_4PbBr_6. *ACS Appl. Energy Mater.* **2020**, *3*, 192−199.
(52) El Ajjouri, Y.; Palazon, F.; Sessolo, M.; Bolink, H. J. Single-Source Vacuum Deposition of Mechanosynthesized Inorganic Halide Perovskites. *Chem. Mater.* **2018**, *30*, 7423−7427.
(53) Lee, J.; Lee, W.; Lee, J.; Baek, K.-Y.; Shin, J.; Kim, J.-K.; Kim, J.; Ahn, H.; Kang, K.; Lee, T. Tailored Design-of-Experiments Approach for Device Performance Prediction and Optimization of Flash-Evaporated Organic−Inorganic Halide Perovskite-Based Photodetectors. *Adv. Mater. Technol.* **2021**, *6*, No. 2001131.
(54) Cao, F.; Yu, D.; Ma, W.; Xu, X.; Cai, B.; Yang, Y. M.; Liu, S.; He, L.; Ke, Y.; Lan, S.; et al. Shining Emitter in a Stable Host: Design of Halide Perovskite Scintillators for X-ray Imaging from Commercial Concept. *ACS Nano* **2020**, *14*, 5183−5193.
(55) Huang, T.; Tan, S.; Nuryyeva, S.; Yavuz, I.; Babbe, F.; Zhao, Y.; Abdelsamie, M.; Weber, M. H.; Wang, R.; Houk, K. N.; et al. Performance-limiting formation dynamics in mixed-halide perovskites. *Sci. Adv.* **2021**, *7*, No. eabj1799.
(56) Lai, M.; Obliger, A.; Lu, D.; Kley, C. S.; Bischak, C. G.; Kong, Q.; Lei, T.; Dou, L.; Ginsberg, N. S.; Limmer, D. T.; Yang, P. Intrinsic anion diffusivity in lead halide perovskites is facilitated by a soft lattice. *Proc. Natl. Acad. Sci. U.S.A.* **2018**, *115*, 11929−11934.
(57) Ke, F.; Wang, C.; Jia, C.; Wolf, N. R.; Yan, J.; Niu, S.; Devereaux, T. P.; Karunadasa, H. I.; Mao, W. L.; Lin, Y. Preserving a robust $CsPbI_3$ perovskite phase via pressure-directed octahedral tilt. *Nat. Commun.* **2021**, *12*, No. 461.

https://doi.org/10.1021/acs.chemmater.3c00833
Chem. Mater. XXXX, XXX, XXX−XXX